

ARTICLE

<https://doi.org/10.1038/s42004-019-0196-2>

OPEN

Functionalization of 2D materials for enhancing OER/ORR catalytic activity in Li-oxygen batteries

Alireza Ostadhossein¹, Jack Guo¹, Filip Simeski¹ & Matthias Ihme¹

A major barrier toward the practical application of lithium-oxygen batteries is the high overpotential caused by the precipitation of oxygen-reduction products at the cathode, resulting in poor cyclability. By combining first-principle calculations and reactive molecular dynamics simulations, we show that surface functionalization of 2D MXene nanosheets offers a high degree of tunability of the catalytic activity for oxygen-reduction and oxygen-evolution reactions (ORR/OER). We show that the controlled creation of active vacancy sites on the MXene surface enhances ORR in excess of a factor of 60 compared to graphene-based cathode materials. Furthermore, we find that increasing the ratio of fluorine vs. oxygen termination of the functionalized Ti_4N_3 -MXene catalyst reduces the charge overpotential by up to 70% and 80% compared with commercial platinum-on-carbon and graphene catalysts, respectively. These results provide direct guidance toward the rational design of functionalized 2D materials for modulating the catalytic activity for a wide range of electrocatalytic applications.

¹Department of Mechanical Engineering, Stanford University, Stanford, CA 94350, USA. Correspondence and requests for materials should be addressed to M.I. (email: mihme@stanford.edu)

Lithium–oxygen (Li–O₂) batteries^{1,2} have attracted significant interest as a promising candidate for rechargeable power sources due to their high theoretical specific energy (3458 Wh/kg) compared with state-of-the-art lithium-ion batteries (265 Wh/kg)³. However, their deployment has been hindered by fundamental challenges such as poor cyclability, large discharge overpotential¹, degradation of the cathode material⁴, and slow oxygen reaction kinetics⁵.

The operation cycle of Li–O₂ batteries involves the oxygen-reduction reaction (ORR) during the discharge and the oxygen-evolution reaction (OER) within the charging process. It is well understood that the kinetics of ORR is sluggish, resulting in a decrease in power density and higher discharge overpotential⁶. Furthermore, products of the reduction step precipitate on the surface of the cathode, leading to high charge overpotential and poor cyclability of the cell due to their insulating characteristics and sluggish kinetics decomposition^{7,8}. Hence, selecting an appropriate catalyst as cathode material is of fundamental importance to promote ORR/OER.

Thus far, various types of carbonaceous materials, such as carbon nanofibers^{9,10}, graphene^{11,12}, functionalized graphene¹⁰, and porous carbon¹³, have been considered as cathodes in Li–O₂ batteries. Among various proposed carbon-based cathode materials, porous carbon loaded with catalytic nanoparticles (either metal or metal oxide) is the most extensively studied material¹⁰. Employing catalytic particles reduces the overpotential, thus leading to enhanced cyclability. Nevertheless, noble metal catalyst particles (such as Au, Pt, and MnO₂) that are typically used in these systems are quite expensive. Furthermore, their catalytic properties are mostly effective in enhancing ORR rather than OER, for which the high overpotential is more crucial¹⁴. In addition, the carbon substrate in these cathode systems is readily oxidized at higher voltage (above 3.0 V)¹⁵, thereby reacting with the discharge products in Li–O₂ batteries to form lithium carbonate (Li₂CO₃)^{16,17}. Therefore, identifying a suitable alternative catalyst cathode to carbonaceous material is one of the greatest challenges.

Carbonate-based electrolyte solvents that are used in Li–O₂ batteries are known to decompose upon cell discharge, giving rise to deposition of Li₂CO₃¹², which acts an insulator by blocking the active sites of the catalyst¹⁸. To alleviate issues concerning the instability of organic carbon-based electrolytes, substantial efforts have been devoted to finding alternative solvents. Alkali metal nitrate molten salt electrolytes (e.g., LiNO₃–KNO₃ eutectic) together with porous carbon cathodes have demonstrated high energy efficiency of ORR through two-electron pathways. In this battery system, the discharge product, lithium peroxide (Li₂O₂), is stable and moderately soluble in the molten salt electrolyte¹⁹. Recently, Xia et al.²⁰ reported a highly reversible four-electron redox Li–O₂ cell that was demonstrated to operate for many cycles at high current rates without appreciable degradation in capacity.

Glyme-based material have been recognized as a promising electrolyte due to their good stability toward the oxidation potential of up to 4.0 V. The employment of glyme and ionic liquid-based electrolytes was found to lower the overpotential and enhance the cycle stability^{21,22}. However, these materials suffer low ionic conductivity, and exhibit limited O₂ solubility. In another effort, the addition of redox mediators (RMs)²³ into the electrolyte solution was recognized to effectively reduce the capacity degradation due to Li₂O₂ precipitation on the cathode surface by transforming the heterogeneous ORR on the cathode surface to the homogeneous one in an electrolyte solution, resulting in improved discharge capacity. In the reverse reaction, they can decrease the lifetime of superoxide in the Li–O₂ battery, leading to the reduction of the overpotential through the 2e[−] pathway. The utilization of RM, such as ethyl viologen (EtV²⁺), was demonstrated to promote the ORR²⁴ and direct

electrochemical decomposition of lithium superoxide (LiO₂) through the OER process²⁵.

The emergence of two-dimensional (2D) materials over recent years has offered a number of promising candidates for improving the electrocatalysis of ORR/OER due to their high specific surface area and high surface density of active catalytic sites. Some materials of interest to Li–O₂ batteries are nitrogen-doped graphene²⁶, hexagonal boron nitride (*h*-BN) on Ni surfaces^{14,27}, and molybdenum carbide (Mo₂C)²⁸. Layered transition metal-carbide and metal-nitride MXenes with the general formula of M_{*n*+1}X_{*n*}, with M being a transition metal and X = {C, N}, are highly stable 2D materials containing 2*n* + 1 layers of atoms²⁹ (see Supplementary Fig. 1, Supplementary Note 1). In the MXene structure, the X-atom that occupies the inner octahedral site covalently bonds with the three-folded transition metal atoms of the outer layers.

The synthesis of MXene involves selective etching of aluminum from the bulk MAX-phase in the presence of various solutions, such as hydrofluoric acid (HF), hydrochloric acid (HCl), sulfuric acid, and other acidic mixtures and fluoride salt. The chemically exfoliated layers are subsequently rinsed with water³⁰. An example of the latter case is a LiF–HCl mixture, resulting in formation of HF during the etching process^{31–33}. Increasing the concentration of LiF can lead to the formation of larger MXene flakes³⁴. This process causes the bare surface of MXene to become functionalized with –O, –OH, and/or –F groups. The formation of functionalized MXene (f-MXene) whose formula is M_{*n*+1}N_{*n*}T₂, with T = {O, OH, F} denoting a functional group, makes the basal plane of MXene more stable³⁵. The large specific surface area of MXene and the flexibility of its surface termination motivate the utilization of MXene as cathode catalyst to mediate ORR/OER in nonaqueous Li–O₂ batteries. MXene offers the benefit of being considerably less expensive compared with precious metal catalysts and exhibits high chemical and mechanical stability while catalyzing ORR and OER^{36–38}. The electric conductivity of MXene due to free electrons of the transition metal and its versatile surface-catalytic chemistry make it a unique material for energy storage, in metal (Li, Na, K, and Ca) ion batteries^{35,39,40}, and for the electrocatalysis in hydrogen evolution reaction³³.

In this study, we investigate the feasibility of modulating the overpotential and power density of nonaqueous Li–O₂ batteries through the functionalization of titanium-based MXene nanosheets as highly tunable cathode catalysts. By combining first-principle calculations using density functional theory (DFT) and reactive molecular dynamics (rMD) simulations, we identify electrocatalytic pathways at the f-MXene surfaces. Specifically, we report that the surface functionalization of the MXene basal plane leads to significantly enhanced catalytic activities and reduced overpotential of ORR and OER. We show that reduced electro-negativity difference between Ti and N, compared with that of Ti and C, along with an increased MXene-sheet thickness and fluorine-surface functionalization reduces the overpotential, η_{tot} , thereby enhancing the catalytic performance. We find Ti₄N₃F₂ with $\eta_{\text{tot}} \approx 1.04$ V to be the most promising candidate for ORR/OER in nonaqueous Li–O₂ batteries. We demonstrate that the enhanced ORR catalytic activity of MXene, which is superior to existing Pt(111) and N-doped graphene catalysts, can be controlled by active vacancy sites on the surface. These results indicate that functionalization in 2D materials is a promising approach for modulating the catalytic activities, thereby enabling the tunability of the overpotential and enhancing the power density of cathode materials in Li-air batteries.

Results

Ab initio thermodynamic analysis of charge and discharge processes at low overpotential. In order to examine the

electrocatalytic performance of MXene surfaces within discharge and charge processes, we first calculate the ORR and OER overpotentials, utilizing the highest level of ab initio simulations based on the PBE/DFT-D2⁴¹ potential in VASP^{42,43}. We compute the adsorption energies of intermediate discharge lithium oxides (Li_pO_q) products for bare and f-MXene ($\text{Ti}_{n+1}\text{X}_n$ and $\text{Ti}_{n+1}\text{X}_n\text{T}_x$, where $n = \{1, 2, 3\}$, $\text{X} = \{\text{C}, \text{N}\}$, and $\text{T} = \{\text{O}, \text{F}, \text{V}\}$ with V denoting a vacant site) surfaces. These DFT simulations (Computational Details) are validated by calculating the structural properties and the stability of bare and f-MXene, and good agreement with previously reported results^{44,45} is obtained (see Supplementary Note 2, Supplementary Table 1). Following the approach used by Yun et al.⁴⁶, the Gibbs free energy of intermediate adsorbate molecules is determined based on their optimized adsorption geometries and the ab initio thermodynamic formalism, which is further explained in the Computational Details.

The ORR/OER overpotentials and adsorption energies of intermediate adsorbate species on the MXene surfaces are computed and reported in Table 1. We compare these results with those of commercial graphene⁴⁷, Pt(111)⁴⁸, h-BN/Ni(111)⁴⁹, and N-doped graphene²⁶ surfaces. The evaluated charge overpotential ($\eta_{\text{OER}} = U_{\text{C}} - U_0$) and discharge overpotential ($\eta_{\text{ORR}} = U_0 - U_{\text{DC}}$) of $\text{Ti}_{n+1}\text{X}_n\text{T}_x$ for $\text{X} = \{\text{N}, \text{C}\}$ and $n = \{1, 2, 3\}$ are presented in Fig. 1a, showing that the surface functionalization leads to a significant reduction of the total overpotential, which is defined as $\eta_{\text{tot}} = \eta_{\text{OER}} + \eta_{\text{ORR}}$. In particular, η_{tot} of $\text{Ti}_4\text{N}_3\text{F}_2$ (1.04 V) is substantially lower than that of $\text{Ti}_4\text{N}_3\text{O}_2$ (1.82 V) and bare Ti_4N_3 -MXene (7.27 V), and decreases with increasing number of atomic layers in the MXene. Furthermore, the calculated overpotentials presented in Table 1 and Fig. 1 show that the total overpotential pertaining to carbon-based MXenes, $\text{Ti}_{n+1}\text{C}_n\text{T}_x$, is notably higher than that of nitrogen-based MXenes, $\text{Ti}_{n+1}\text{N}_n\text{T}_x$. This can be attributed to the lower charge density of $\text{Ti}_{n+1}\text{C}_n$ around the functional groups. It is noted that due to the larger difference in electronegativity between Ti and N compared with that between Ti and C, stronger charge delocalization from the functional groups to the surrounding Ti atoms is induced (see Supplementary Fig. 5 for illustration of the charge density distribution). The lowest total overpotential of the F-terminated MXene is attributed to the lowest adsorption energy of Li_pO_q adsorbates on the fully fluorinated MXene surface, demonstrating the effective catalytic activities of these materials for OER and ORR. Based on the charge density distributions of Ti_3N_2 , the adsorption of a LiO_2 -molecule causes a reduced charge density around the surface Ti atoms, which is consistent with the charge localization on the Li- and O-atoms of LiO_2 , leading to the improved electron environment for catalyzing the ORR. In contrast, the electron delocalization from the Ti and O-atoms on the surface of the O-terminated MXene shows that the adsorption of LiO_2 results in a redistribution of the electronic structure, which leads to lower adsorption energy of LiO_2 intermediate, and thereby lower overpotential for OER catalysis (see Supplementary Fig. 4). Figure 1b–d displays free energy diagrams along the OER and ORR pathways with the most stable adsorption configurations on the bare, O-terminated, and F-terminated $\text{Ti}_4\text{N}_3\text{T}_x$ MXene surfaces. In these diagrams, the Gibbs free energies are evaluated based on the energy of O_2 and ($\text{Li}^+ + \text{e}^-$) obtained from an isolated O_2 molecule and Li atom in the Li-bcc bulk. It is noted that the free energies in Fig. 1 are translated by the free energy of four Li^+ ions and an O_2 molecule so that the equilibrium potential is represented as applied voltage, i.e., $U = 0.0$ V at standard conditions. The OER curves are obtained by shifting the standard Gibbs free energies, ΔG^0 , by the amount of $m\text{e}U$, where m denotes the number of transferred electrons. We calculate the charge and discharge voltages (U_{C} and U_{DC} ,

respectively) defined as the lowest and the highest voltage that maintains each pathway downhill. It can be seen that among all calculated MXene surfaces, fluorinated MXene exhibits the best electrochemical performance. Specially, with $U_{\text{C}} = 3.07$ V, it has remarkably better OER catalytic performance as compared with bare ($U_{\text{C}} = 8.7$ V) and oxygenated ($U_{\text{C}} = 3.85$ V) MXenes. In this context, it is noted that the role of the electrolyte and temperature have not been considered in the calculation presented in Table 1. Although at ambient condition, the 2e^- ORR pathway is thermodynamically and kinetically more favorable, by tuning the operating temperature and employing appropriate electrolyte, an electrochemically reversible formation of Li_2O instead of Li_2O_2 can be achieved. Recently, a remarkable recyclability with an overpotential of 0.2 V was reported by utilizing a stable inorganic $\text{LiNO}_3/\text{KNO}_3$ liquid electrolyte and a bifunctional metal oxide catalyst²⁰.

Role of surface vacancies to mediate catalytic activities of MXene during discharge. To gain a fundamental understanding about the role of the surface structure of MXene cathode catalysts on mediating the power density, a kinetic analysis is performed by employing rMD simulations using a ReaxFF force field⁵⁰. We choose the ReaxFF force field because it is well suited to study the energetics of multiphase systems especially in catalytic reactions and because of its demonstrated capability in modeling the catalytic behavior of metal oxide nanoparticles for PdO_2 ⁵¹, CeO_2 ⁵², and TiO_2 ⁵³. The ReaxFF force field parameters are trained to describe Ti/N/Li/O interactions, and the potential is based on an existing parameter set that was validated for studying the intercalation of cations on Ti-C MXene surfaces in aqueous environments⁵⁴. The detailed description of the developed force field together with the training and validation procedures are provided in Supplementary Note 3.

We consider the abundant MXene surface to be terminated with different coverage ratios of O- and F-functional groups. In addition to studying the effect of the partial pressure of O_2 on the ORR rates, we prepare the homogeneous mixture of Li and O_2 in four different composition ratios of $\alpha = N(\text{O}_2)/N(\text{Li}) = \{0.125, 1.0, 2.0, 4.0\}$.

In these simulations, the formation rate of discharge products is analyzed assuming that the dissociation of O_2 molecules gives rise to the formation of Li_2O_2 through the global reaction $2\text{Li} + \text{O}_2 \rightarrow \text{Li}_2\text{O}_2$ (see Computational Details). This assumption was validated by studying the kinetic behavior of ORR in the bulk phase, consisting of a Li/ O_2 mixture. The ORR rate of the bulk-phase reaction predicted by this model was found to be in good agreement with experimental measurements (see Supplementary Fig. 7).

Snapshots of the rMD simulations at the end of the calculation for a temperature of 300 K are illustrated in Fig. 2. In these simulations, a free-standing single-layer $\text{Ti}_3\text{N}_2\text{T}_x$ MXene sheet is placed in the center of the simulation box in contact with the Li/ O_2 mixture in the bulk phase. It is observed that throughout the simulation over 150 ps, O_2 molecules react with Li atoms either in the bulk phase or at the MXene surface leading to the formation of Li_pO_q compounds. It is worth noting that when the surface of MXene is not functionalized (see Fig. 2a) the number of unreacted O_2 molecules in the bulk phase is markedly less than that covered by O- (Fig. 2b) and F-termination groups (Fig. 2c).

The principal surface reaction steps, observed from the rMD simulations, are shown below the final configurations of Fig. 2. For bare MXene (Fig. 2a), O_2 dissociates at the surface (9.75 ps) upon which a chemisorbed O atom reacts with two Li atoms to form Li_2O (10.5 ps). The Li_2O -complex recombines with neighboring O atoms to form Li_2O_2 (17.35 ps), and proceeds

Table 1 Overpotential and adsorption energies during discharge (ORR)/charge (OER) process

	η_{ORR}	η_{OER}	η_{tot}	$\Delta G_{\text{Li}_2\text{O}_2}^{\text{O}}$	$\Delta G_{(\text{Li}_2\text{O}_2)^*}^{\text{O}}$	$\Delta G_{(\text{Li}_2\text{O}_2)_2}^{\text{O}}$	$\Delta G_{(\text{Li}_2\text{O}_2)_3}^{\text{O}}$
Ti ₄ N ₃	4.92	2.36	7.28	10.93	6.81	16.49	7.23
Ti ₄ N ₃ O ₂	0.61	1.22	1.83	1.23	2.05	3.77	2.97
Ti ₄ N ₃ F ₂	0.59	0.45	1.04	6.37	0.99	0.96	1.93
Ti ₄ C ₃	5.24	3.71	8.95	11.57	7.23	17.15	8.59
Ti ₄ C ₃ O ₂	2.09	0.66	2.75	1.78	2.23	4.26	3.47
Ti ₄ C ₃ F ₂	1.25	0.98	2.23	7.24	1.29	1.32	2.43
Graphene ⁴⁷	1.35	2.16	3.51				
Pt(111) ⁴⁸	1.02	1.62	2.64				
<i>h</i> -BN/Ni(111) ⁴⁹	1.15	0.74	1.89	4.04	4.77	8.43	4.80
N-doped graphene ^{26,47}	0.89–1.66			1.01	1.21	2.38	0.56

The ORR overpotential, η_{ORR} , OER overpotential, η_{OER} , and the adsorption energies, ΔG_{ads} , of lithium oxides (Li_{*p*}O_{*q*}) are evaluated for both bare and functionalized Ti₄N₃T_{*x*} and Ti₄C₃T_{*x*} MXene surfaces; reported results of commercial cathode materials^{47–49} are included for reference

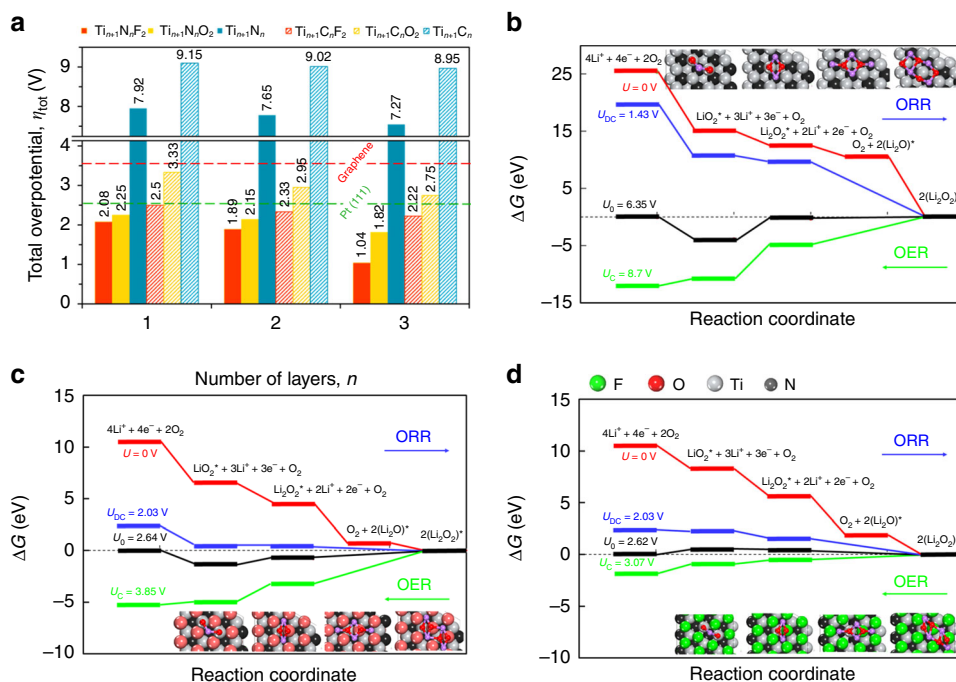


Fig. 1 Electrochemical performance of Ti-based MXenes for ORR/OER. **a** Comparison of total overpotential, η_{tot} , for MXene surfaces as a function of the number of atomic layers, *n*, and functional groups. The calculated overpotentials of functionalized MXene surfaces are significantly smaller than those of bare MXenes. Minimum energy pathways and optimized geometries of the adsorbed lithium oxides on **b** bare and **c** O- and **d** F-terminated MXenes (see Supplementary Note 4 for the mixture of O and F terminations). The 2e⁻ pathway is predicted to be the preferred reaction mechanism for all cases. Blue and green lines denote the reaction steps for the intermediate discharge and charge product adsorption on MXene surfaces, respectively. The asterisk symbol denotes an adsorbed state of ORR intermediates

with the agglomeration into larger Li₂O₂ clusters (132.5 ps). The Li₂O₂ formation on fully functionalized O-MXene surfaces (Fig. 2b) is initiated by the diffusion of Li toward the hollow sites and the chemisorption via the formation of three covalent bonds with neighboring O-termination groups (1.25 ps). This is followed by the reaction with an O atom in the gas phase (2.75 ps) to form Li₂O; the Li₂O combines with another Li atom to form Li₂O₂ (3.5 ps), leading to the formation of larger Li₂O₂ clusters (141 ps). In contrast to these chemisorption processes, our calculations show that O₂ is physisorbed on the F-terminated MXene surface (Fig. 2c, 14.75 ps), which is followed by the formation of Li_{*p*}O_{*q*} complexes through the reaction of Li with physisorbed O₂ or O₂ in the bulk (59.75 and 76.25 ps), and the separation from the surface (112.5 ps).

To examine the surface-mediated ORR kinetics, ternary diagrams for the Li/O₂ electrochemical reaction on MXene surfaces are

presented in Fig. 3. Every point on these plots represents a different MXene surface composition, which is either vacant (V) or terminated by oxygen (O), fluorine (F), or by a mixture of both. The coverage of each termination group is varied between 0 and 100%. Vertices of each triangle represent a fully covered MXene surface. As will be described later, the ORR reaction in contact with OH-terminated MXene will not be studied here, since it was found not to be a suitable cathode material due to the hydroxide dissociation and the subsequent formation of H₂. From this viewpoint, OH-terminated MXene might be more suitable for the catalysis of Li-O₂ batteries with aqueous electrolytes. The electrochemical ORRs in the presence of an aqueous electrolyte and OH-terminated MXenes can lead to the formation of LiOH and potentially compensate peeling the H-atom from the OH-terminated MXene surface as observed from the GCMC-rMD simulations in Supplementary Fig. 10 and Supplementary Note 5.

To demonstrate the superior catalytic performance of MXene surfaces in accelerating the reaction of Li and O₂, we report ORR rates nearby MXene surface, k_{MXene} ; these rates are normalized by those obtained from ORR on pristine graphene catalyst surfaces, k_{Gr} , at otherwise identical conditions. Graphene is a prevalent cathode material due to its highly catalytic active surface and large specific surface area^{10,55}. The homogeneous structure of pristine graphene, which only consists of carbon atoms in the sp²-hybridized state, facilitates a direct comparison between the reaction rates of various f-MXene materials. To facilitate a direct comparison, we determine the relative reaction rate constant, $\bar{k} = k_{\text{MXene}}/k_{\text{Gr}}$, by performing two simulations with identical Li/O₂ mixture composition on MXene and graphene (see Computational Details for the procedure of evaluating the ORR rates). The influence of partial pressure on the kinetics of ORR is examined by changing the O₂:Li ratio in Fig. 3a–c. The results show that, irrespective of the partial pressure of O₂, Ti₃N₂T₂-MXene surfaces exhibit at least a fivefold increase in the ORR rates (compared with the state-of-the-art graphene catalysts), indicating that the basal plane of Ti₃N₂T₂-MXene is electrocatalytic active for ORR enhancement. As illustrated in Fig. 3a–c, among all studied surface-termination compositions, vacancies provide the most effective surface sites for enhancing ORR. Compared with bare and partially f-MXene, increasing the surface functionalization reduces the effective catalysis sites, which results in a reduction in the effective ORR rate (see Fig. 3f). The kinetic analysis of Fig. 3a–c further shows that unterminated MXene surfaces deliver a high exchange current density and therefore enhanced power density compared with fully O- and F-terminated MXene. These results also indicate that for partially terminated MXenes synergistic effects of vacancies with neighboring F- and O-termination groups provide active sites for the O₂ dissociation. The enhanced ORR kinetics achieved by introducing vacancy sites on the surface of MXene (Supplementary Table 3) suggest that the basal plane of MXene, which is often functionalized by F- and O-termination groups, is highly tunable for achieving enhanced power density and ORR catalysis by controlling the population of vacancy defects on the surface.

Analysis of the temporal evolution of ORR (see Supplementary Fig. 10) shows that Li₂O₂ species are rapidly formed (within the first 40 ps). However, the initial Li₂O₂ formation through the dissociation of O₂ slows down and reaches an equilibrium state after approximately $t = 150$ ps. It is worth noting that the trajectories of our rMD simulations and the species evolutions (Supplementary Fig. 9) show that the final ORR products contain a combination of Li₂O and Li₂O₂. The coexistence of these compounds indicates that ORR involves the disproportionation reaction^{16,56,57} by which Li₂O₂ is converted to Li₂O and O₂. In particular, when the basal plane of MXene is fully functionalized with fluorine, we observe that small clusters of LiO₂, which are formed near the surface, diffuse into the bulk phase and react with the remaining Li and O₂. A portion of the Li₂O₂ that detaches from the catalyst surface participates in the chemical disproportionation reaction.

Examining the effect of partial pressure on the ORR rates (Fig. 3) shows that the efficiency of the electrochemical catalysis is significantly affected by the increase in partial pressure of oxygen. In particular, when the MXene surface is terminated by a particular functional group, the ORR rate increases with increasing O₂:Li ratio, and is highest for $\alpha = 4$. This trend is consistent with the experimentally reported ORR kinetic behavior over Pt catalyst surfaces⁵⁸. However, near bare MXene, ORR is found to become slower at higher O₂:Li ratio (see Supplementary Table 2).

The dependence of the ORR kinetic rates on temperature is examined by considering Arrhenius plots in Fig. 3d, e. It can be seen that for fully and partially f-MXenes, the ORR process is endothermic (Fig. 3f). The reduced rates in the presence of O/F-terminated MXenes are attributed to a less adsorptive dissociation of the O₂-molecules near F- and O-termination groups compared with that near the bare MXene surface, leading to a higher Li/O₂ reaction rate in the gas phase. Nevertheless, when the MXene surface is partially functionalized, even the presence of few vacancy sites on the basal plane significantly alters the ORR kinetics to an exothermic behavior. Due to higher dissociation rates of the reaction between the dissolved O₂ molecules and the active vacancy sites, the ORR process over the vacancy-rich MXene surfaces becomes more exothermic. Consequently, fully f-MXenes are not a suitable materials for ORR catalysis. However, due to the low charge overpotential (Fig. 1), they are efficient catalysts for OER.

To assess the kinetic barriers, we compute the apparent electrochemical activation energies (ΔE_a). As depicted in Fig. 3f, for the homogeneous Li-O₂ mixture and fully f-MXene, the calculated activation energy is positive. In contrast, increasing the concentration of vacancy sites up to 25% may result in a reduction of the apparent activation energy from 450 meV to -50 meV (100 meV to 5 meV) over the partially oxygenated (fluorinated) MXenes. This indicates that the formation of vacancies in F-terminated MXenes leads to the more efficient promotion of ORR. A further increase in the concentration of vacancy sites only has a marginal effect on the reduction of the ORR activation barrier. The functionalization of MXene with F- and O-termination groups increases the ORR activation barrier. In particular, at fully functionalized surfaces, the activation energy is always positive, however, increasing the coverage ratio of F vs. O results in a slight reduction in ΔE_a .

The results presented in Fig. 3 demonstrate that for practical applications, the ORR rate and with this the exchange current density and power density of the discharge process can be actively modulated by the surface coverage of the MXene catalyst. The increase in the surface area of electrochemically active vacancy sites results in a faster ORR. These significant advantages of the Ti-based MXene, including the low overpotential of its functionalized surfaces and the tunable catalytic activities due to the formation of surface vacancy sites, are superior to most cathode-catalyst materials that are commonly employed for Li-O₂ batteries, such as doped graphene or Pt-based catalysts.

Electrochemical reaction mechanisms during ORR near MXene catalyst surfaces. Based on the DFT and rMD results, we propose the following principal ORR mechanism at the MXene catalyst surfaces (Fig. 4). Depending on the surface terminations of MXene the peroxide-mediated pathways involve the following steps.

1. ORR on bare MXene (Fig. 4a):

- Step i—Adsorptive dissociation of oxygen: Upon discharge, both Li and O₂ diffuse toward the active vacancy sites. Due to the higher adsorption energy, O₂ chemisorbs on the surface: $\text{O}_2 \rightarrow 2\text{O}^*$.
- Step ii—Lithiation: The adsorbed oxygen is electrochemically reduced and reacts with Li to form lithium oxide: $2\text{O}^* + \text{Li}^+ + \text{e}^- \rightarrow (\text{LiO}_2)^*$.
- Step iii—Lithium-peroxide nucleation: Small clusters of Li₂O₂ nucleate at the surface of bare MXene through an electrochemical reaction between adsorbed lithium superoxide and the MXene surface: $(\text{LiO}_2)^* + \text{e}^- + \text{Li}^+ \rightarrow (\text{Li}_2\text{O}_2)^*$. The overall Li₂O₂ nucleation reaction can be regarded as a

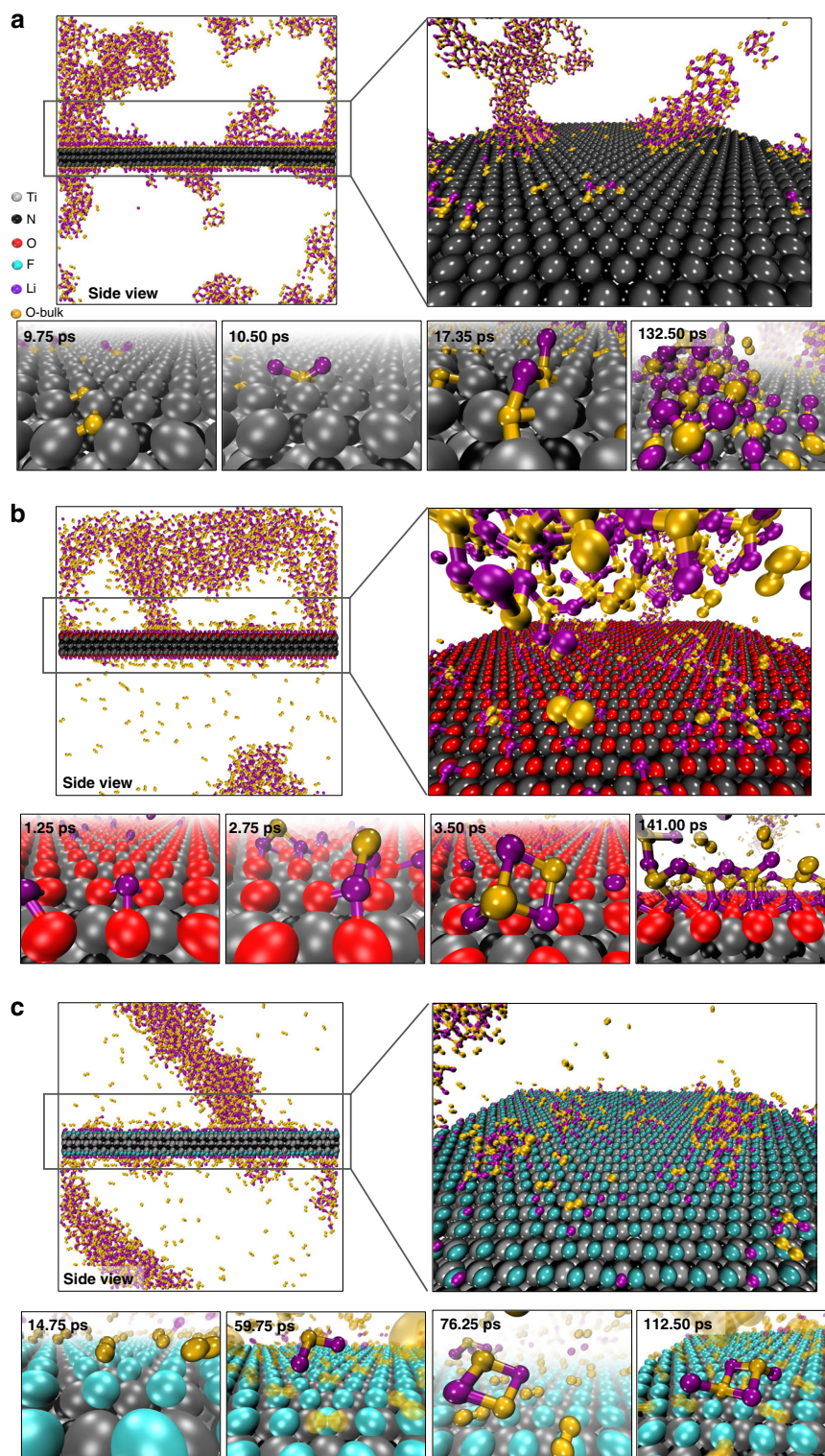


Fig. 2 Reaction steps for oxygen-reduction reaction near bare and functionalized MXene ($\text{Ti}_3\text{N}_2\text{T}_x$) surfaces computed from rMD simulations. Snapshots from rMD simulations at $T = 300$ K, associated with the final configuration of atoms during ORR **a** bare **b** fully O-terminated, and **c** fully F-terminated MXene surfaces. To differentiate between O atoms in the bulk-phase and O-termination groups, oxygen originating from the bulk phase is color coded as yellow, and the surface oxygen is shown in red

- combination of the two elementary reactions from step ii and step iii, through a two-electron transfer mechanism.
 - Step iv—Precipitation: Larger clusters of Li_2O_2 are formed due to the agglomeration of small Li_2O_2 clusters that are anchored to the bare MXene surface.
2. ORR on O-terminated MXene (Fig. 4b):
 - Step i—Lithiation: Li is first chemisorbed on the oxygenated surface due to its higher adsorption energy compared with that of O_2 : $\text{Li} \rightarrow \text{Li}^+$. The preferred adsorption site for Li is on

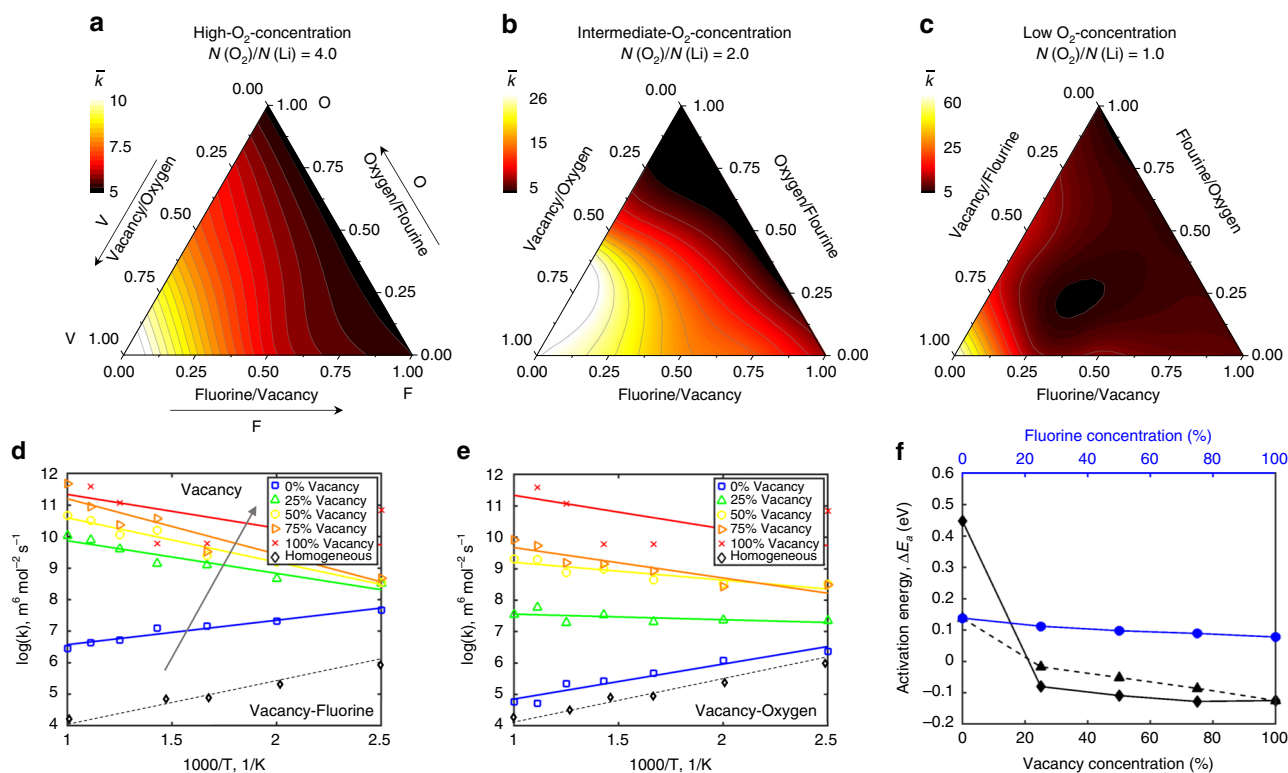


Fig. 3 Ternary plots of ORR kinetics on $\text{Ti}_3\text{N}_2\text{T}_x$ MXene catalyst surface covered by various functional groups. The results are presented for **a** high, **b** intermediate, and **c** low O_2 concentrations at 300 K. The overall reaction rate increases by increasing the bare MXene surface, strongly indicating that vacancies are preferred active sites for promoting ORR catalysis. **d**, **e** Temperature-dependent ORR rate in Arrhenius form for binary mixtures and **f** activation energy as a function of surface vacancy for $\alpha = 1$

top of the X-atom (see Supplementary Fig. 2, Supplementary Note 1).

- Step ii—Oxygen chemisorption: Oxygen is adsorbed on the lithiated surface to form lithium superoxide: $\text{Li}^+ + \text{O}_2 \rightarrow (\text{LiO}_2)^*$.
- Step iii—Lithiation: In the presence of an excess of Li^+ through the reaction with the intermediate $(\text{LiO}_2)^*$ complex, Li_2O_2 is formed: $(\text{LiO}_2)^* + e^- + \text{Li}^+ \rightarrow (\text{Li}_2\text{O}_2)^*$. Compared with ORR on bare MXenes, the electron charge transfer between the Li_pO_q -adsorbates and the O-terminated surface is weak.
- Step iv—Desorption: The large clusters of Li_2O_2 desorb from the surface into the bulk Li/O_2 mixture.

3. ORR on F-terminated MXene (Fig. 4c):

- Step i—Oxygen physisorption: On the fluorinated MXene surface, O_2 is physisorbed to the surface via weak van der Waals forces.
- Step ii—Lithium oxidation: Li reacts with O_2 in the bulk phase to form LiO_2 : $\text{O}_2 + \text{Li} \rightarrow \text{LiO}_2$. There is a small charge transfer between the F-terminated surface and the adsorbed O_2 -molecule.
- Step iii—Lithium-peroxide nucleation: The LiO_2 molecules weakly bind to the surface, and charge transfer happens between Li and F from the surface: $\text{LiO}_2 \rightarrow (\text{LiO}_2)^*$.
- Step iv—Lithium-peroxide desorption: The LiO_2 molecule that is loosely bonded to the surface reacts with another Li atom to form Li_2O_2 : $(\text{LiO}_2)^* + e^- + \text{Li}^+ \rightarrow \text{Li}_2\text{O}_2$. Since Li_2O_2 detaches from the surface and diffuses into the bulk, ORR near the fluorinated MXene surface mainly proceeds within the gas phase rather than the surface-controlled reaction.

The bare surface of MXene provides active sites for the ORR process (Fig. 4a). By receiving electrons from the conductive MXene, the basal plane is capable of reducing O_2 molecules faster than the O/F-terminated surfaces. As a result of the enhanced electron transfer, the rate of ORR, and thus the power and current density of the battery increases, which is confirmed by Fig. 3 and Supplementary Fig. 9). The rate limiting step for O-terminated MXenes is the lithiation step. In contrast, since the electron transfer between the F-terminated MXene surface and Li_pO_q is reduced (Fig. 4c), the Li_2O_2 molecules that are weakly bonded to the surface diffuse into the bulk phase, reducing the effectiveness of the catalyst surface and reduced reaction rates.

Effect of surface potential on the discharge process. In order to quantify the stability of the ORR product and to investigate the potential of utilizing MXene as a cathode for Li- O_2 batteries, we construct a phase diagram in Fig. 5, showing that N-based MXene adsorbs intermediate discharge products through the thermodynamically favorable $2e^-$ pathway, leading to the formation of $2(\text{Li}_2\text{O}_2)$. In analogy to previous analysis on hydrogen electrodes in fuel cells⁵⁹, the effect of voltage, U , is considered by shifting the chemical potential of electrons by $-meU$, i.e., $\Delta G = \Delta G^0 - meU$, where m is the number of electrons and e is an electron charge. This technique has been successfully used for understanding catalysis activities of Pt (111) and Au(111) surfaces in ORR/OER⁶⁰. Figure 5a shows that the first lithiation step of ORR on O-MXene, i.e., the formation of LiO_2 , occurs below 4.03 V. However, the second ORR step is not spontaneous. Rather, the Li_2O_2 nucleation is initiated when the electrode potential drops to 2.08 V. In contrast,

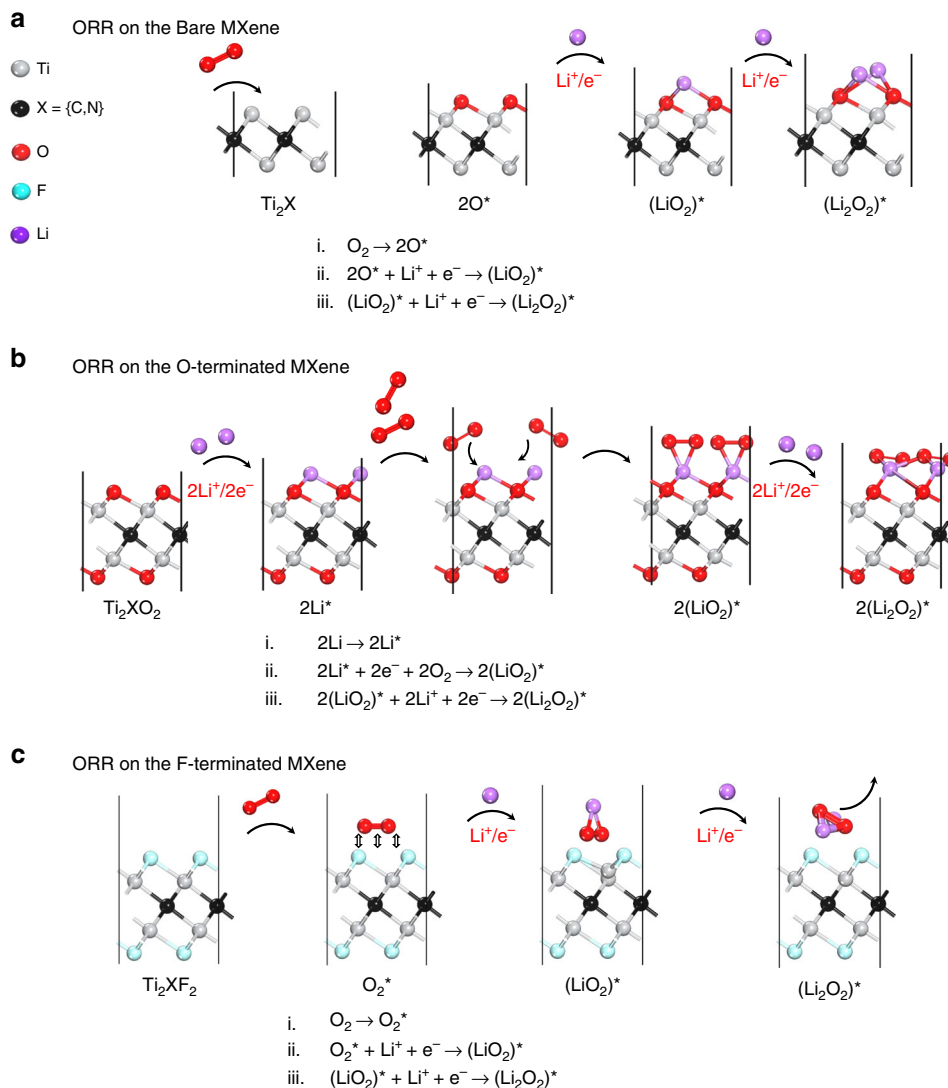


Fig. 4 Illustration of the principal ORR pathways for the O_2 reduction near the MXene catalyst surfaces. ORR mechanism for **a** bare, **b** O-terminated, and **c** F-terminated MXenes

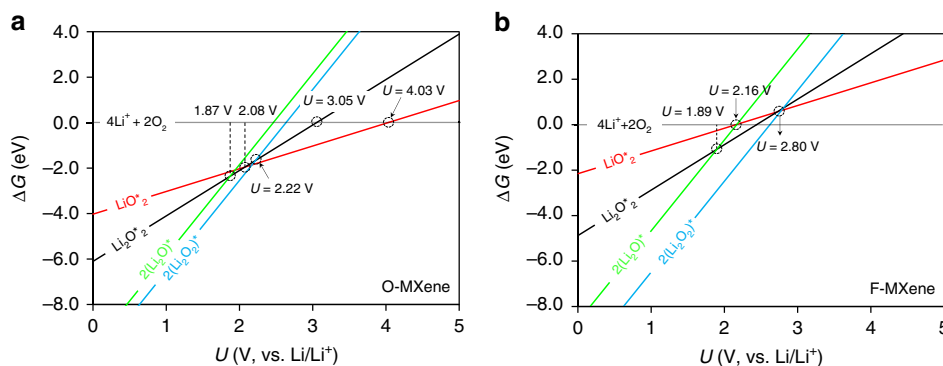


Fig. 5 Phase diagram of Li- O_2 for functionalized MXene surfaces. Potential-dependent profiles of intermediate discharge adsorption to the surface of **a** oxygenated ($\text{Ti}_3\text{N}_2\text{O}_2$) and **b** fluorinated ($\text{Ti}_3\text{N}_2\text{F}_2$) MXene. The zero point of the free energy axes corresponds to the energy of four Li^+ atoms and four O_2 molecules. The intersections are marked with circles to indicate the potential of each reaction step

on the F-terminated MXene surface, both LiO_2 and Li_2O_2 nucleate nearly simultaneously below 2.16 V (see Fig. 5b). The third ORR step on O- and F-terminated MXenes, which is the formation of $(\text{Li}_2\text{O}_2)^*$ and $2(\text{Li}_2\text{O}_2)$, occurs below 1.87 and 1.89

V, respectively. This is represented by the lower stability of $(\text{Li}_2\text{O}_2)^*$ and $(\text{LiO}_2)^*$ at $U > 1.87$ V, which is close to the maximum discharge potential of noble metals, such as Pt and Cu(111) (≈ 1.99 V)⁴⁶.

Contrary to the discharge process by which ORR proceeds through the intermediate adsorption of Li_pO_q , the charging process takes place directly by the decomposition of Li_2O_2 at the interface of the electrolytes and Li_2O_2 within the OER process. According to the phase diagrams of Fig. 5, beyond 2.22 and 2.8 V, which are the intersections of $2(\text{Li}_2\text{O}_2)^*$ and $(\text{Li}_2\text{O}_2)^*$ lines for O-terminated and F-terminated MXenes, respectively, $2(\text{Li}_2\text{O}_2)$ dissociates to Li_2O_2 , 2Li , and O_2 . These threshold potentials can be regarded as the minimum charge potentials, which were calculated in Fig. 1. The lower charge potential of F-terminated MXene compared with that of O-terminated MXene strongly indicates that Li_2O_2 separates easier.

In summary, we have proposed MXene nanosheets as novel and highly tunable 2D materials for the cathode-catalyst of Li- O_2 batteries. Through comprehensive mechanistic studies, employing first-principle calculations and reactive molecular dynamics simulations, the favorable reaction pathways for the adsorption of discharge and charge products have been identified. We found that ORR on both bare and f-MXenes proceeds by the $2e^-$ pathway. Our calculations demonstrate that functionalization of MXene significantly enhances the catalytic activities of MXene for OER, while the formation of vacancies on the already f-MXene surfaces improve the ORR kinetics by more than a factor of 60 compared with that of graphene-based cathode materials.

These results provide new understanding of the influence of surface functionalization of 2D electrodes to control the electrochemical activity in nonaqueous Li- O_2 batteries, thereby paving the way toward the rational engineering of catalyst surfaces for ORR/OER processes.

Methods

Quantum mechanical calculations. Plane wave DFT calculations are conducted using the projector augmented-wave (PAW) method⁶¹. To examine the electronic exchange correlation function of electrons, the Perdew–Burke–Ernzerhof (PBE) exchange functional with generalized gradient approximation is used. In addition, the DFT-D2 approach is used to consider van der Waals interactions. The valence electrons from the 2s orbital for Li, and $3d^2 4s^2$, $2s^2 2p^3$, $2s^2 2p^5$, $2s^2 2p^4$, and $1s^1$ for Ti, N, F, O, and H are expanded on a plane wave basis set. Kinetic energy cut off of 520 eV is used. It is iterated over self-consistent loops until the total energy difference between two adjacent steps is less than 10^{-4} eV. The structure is relaxed until forces are in the range of 0.02 eV/Å. The Brillouin zone is sampled using $8 \times 8 \times 1$ k -points mesh generated based on the Γ -centered Monkhorst–Pack approach⁶². The simulations employ 3×3 super cells for investigating the adsorption mechanisms, corresponding to chemical stoichiometries of $\text{Ti}_{18}\text{N}_9\text{T}_x$, $\text{Ti}_{27}\text{N}_{18}\text{T}_x$, and $\text{Ti}_{36}\text{N}_{27}\text{T}_x$, where $T = \{\text{O}, \text{F}, \text{OH}\}$ with Li, O_2 , LiO_2 , Li_2O_2 , $2(\text{Li}_2\text{O}_2)$, and $2(\text{Li}_2\text{O})$ adsorbate species. The vacuum space for the DFT calculations is considered to be ~ 15 Å on each side.

Ab initio thermodynamic analysis. Free energy diagrams are constructed based on the adsorption energies pertinent to the most stable configuration of the ORR intermediate products, i.e., $(\text{LiO}_2)^*$, $(\text{Li}_2\text{O}_2)^*$, $2(\text{Li}_2\text{O}_2)^*$, and $2(\text{Li}_2\text{O})^*$. The Gibbs free energies of these molecules through the electrochemical adsorption reactions are calculated using the following expression:

$$\Delta G = \Delta E_{\text{tot}} + \Delta E_{\text{ZPE}} - T\Delta S, \quad (1)$$

where ΔE_{tot} denotes the change in total energy obtained from DFT, ΔE_{ZPE} , and ΔS are the changes of the zero-point energy and the entropy at standard conditions ($T = 298$ K and at potential of 0 V vs. Li/Li^+ reference electrode for O_2 reduction).

Following Lee et al.⁶³, intermediate reaction steps can be categorized based on their preference for Li and O_2 adsorption, such that

$$\Delta G_f^0 = G_{\text{Li}_p\text{O}_q}^0 - pG_{\text{Li}}^0 - \frac{q}{2}G_{\text{O}_2}^0, \quad (2)$$

The adsorption energies of Li_pO_q intermediates, for a given site, are defined as

$$E_{\text{ads}} = E_{\text{surf}+\text{Li}_p\text{O}_q} - E_{\text{surf}} - E_{\text{Li}_p\text{O}_q}, \quad (3)$$

where E_{surf} is the energy of the surface, $E_{\text{Li}_p\text{O}_q}$ is the energy of molecular Li_pO_q species, and $E_{\text{surf}+\text{Li}_p\text{O}_q}$ is the total energy of the system.

It is worth noting that in this method, the lower adsorption energy values, E_{ads} , implies stronger binding between adsorbate molecules and MXene surface. The equilibrium potential for bulk Li-bcc metal, Li_2O_2 (Föpl structure), and Li_2O (antifluorite structure) are obtained from the standard free energies of formation

with the following equation:

$$U_{\text{eq}} = -\frac{1}{ne} \left[\Delta G_f^0(\text{Li}_2\text{O}_{2(s)} \text{ or } \text{Li}_2\text{O}_{(s)}) \right]. \quad (4)$$

Since volume and entropy changes are negligible for a solid-state reaction, the change in free energy is approximated by the internal energy change ΔE .

rMD simulations. The rMD simulations are carried out on a mixture of Li and O_2 nearby the surface of bare, and f-MXene sheets. MXene nanosheets contain 40×30 unit cells. In these calculations, Li and O_2 molecules are homogeneously dispersed in a simulation box, with the lateral dimensions ($96.7 \text{ \AA} \times 83.4 \text{ \AA} \times 100.0 \text{ \AA}$), corresponding to the x -, y -, and z -direction, respectively. The number of Li atoms is set to be fixed with $N(\text{Li}) = 2000$. However, the ratio of O_2 vs. Li is varied to study the influence of oxygen partial pressure.

Periodic boundary conditions are applied along all three directions. The system properties and concentration ratios are chosen to represent experimental operating conditions of Li- O_2 batteries⁵⁷. For each case, the atomic configuration is equilibrated at constant temperature, ranging from $T = 200$ to $T = 1000$ K, in increments of 100 K. Prior to performing rMD simulations, the potential energy of the system is minimized to avoid simulation artifacts that are usually caused by excessive close-range and high-energy interactions of atoms. All rMD simulations are performed using the LAMMPS package^{64,65} in conjunction with a newly developed ReaxFF force field (see Supplementary Note 2). A small time step of 0.25 fs is chosen to ensure that the total energy of the system is conserved within the simulation time frame. The temperature of all rMD simulations is controlled by employing a canonical (NVT) ensemble using Nos–Hoover thermostat with temperature damping constant of 25.0, and the velocity Verlet algorithm is used to integrate the phase space.

Evaluation of the reaction rate constants. To determine the reaction rates, we consider the Li_2O_2 formation through the third-order reaction:



with the law of mass action

$$\frac{1}{2} \frac{d[\text{Li}]}{dt} = \frac{d[\text{O}_2]}{dt} = -k[\text{Li}]^2[\text{O}_2]. \quad (6)$$

By introducing the stoichiometric relations for O_2 and Li consumption during ORR⁶⁶

$$f_s = \frac{[\text{Li}]_0 - [\text{Li}]}{[\text{O}_2]_0 - [\text{O}_2]}, \quad (7)$$

the reaction rate constant, k , can be determined as

$$\left(1 - f_s \frac{[\text{O}_2]_0}{[\text{Li}]_0}\right) \left(1 - \frac{[\text{Li}]_0}{[\text{Li}]}\right) + \ln\left(\frac{[\text{Li}][\text{O}_2]_0}{[\text{Li}]_0[\text{O}_2]}\right) = kt([\text{Li}]_0 - f_s[\text{O}_2]_0)^2 \quad (8)$$

where the subscript ‘0’ denotes the initial concentration.

Grand canonical Monte Carlo (GCMC). To further validate the ReaxFF potential description, the open circuit voltage (OCV) is calculated based on a combined GCMC and intermediate rMD simulations. For this purpose, a super cell, consisting of $2 \times 2 \times 1$ unit cells of $\text{Ti}_3\text{N}_2(\text{OH})_2$ and $\text{Ti}_3\text{N}_2(\text{OH})_2$, is employed. As discussed in Supplementary Note 5, Li atoms from a fictitious reservoir, with chemical potential $\mu_{\text{Li}} = -1.62$ eV (cohesive energy of Li in Li-bcc), are deposited on the O- and OH-MXene surfaces. During the GCMC simulation, the temperature, $T = 300$ K, and the chemical potential of the reservoir are maintained under a μ - P - T ensemble. This condition allows the cell dimensions to be relaxed along the basal-plane directions.

Data availability

Kinetic Study of ORR in the bulk phase, validation of DFT simulations, potential adsorption site on f-MXenes, the ReaxFF force field and DFT calculated values for adsorption energy, binding energies and equation of states of bare and functionalized Ti-N MXenes, the configuration of Li intercalated MXene using GCMC, adsorption energies, and OCV of f-MXene surfaces. Activation energy associated with ORR near MXene with various termination groups and coverages, and the electron difference density of Li_pO_q adsorbed on MXene surface.

Received: 15 April 2019 Accepted: 22 July 2019

Published online: 13 August 2019

References

1. Girishkumar, G., McCloskey, B., Luntz, A. C., Swanson, S. & Wilcke, W. Lithium-air battery: promise and challenges. *J. Phys. Chem. Lett.* **1**, 2193–2203 (2010).
2. Bruce, P. G., Freunberger, S. A., Hardwick, L. J. & Tarascon, J.-M. Li- O_2 and Li-S batteries with high energy storage. *Nat. Mater.* **11**, 19–29 (2012).

- Luntz, A. C. & McCloskey, B. D. Nonaqueous Li-air batteries: a status report. *Chem. Rev.* **114**, 11721–11750 (2014).
- Ottakam Thotiyl, M. M., Freunberger, Z., Peng, S. A., Chen, Y. & Liu, Z. A stable cathode for the aprotic Li-O₂ battery. *Nat. Mater.* **12**, 1050–1056 (2013).
- McCloskey, B. D. et al. Limitations in rechargeability of Li-O₂ batteries and possible origins. *J. Phys. Chem. Lett.* **3**, 3043–3047 (2012).
- Sun, B., Huang, X., Chen, S., Munroe, P. & Wang, G. Porous graphene nanoarchitectures: an efficient catalyst for low charge-overpotential, long life, and high capacity lithium–oxygen batteries. *Nano Lett.* **14**, 3145–3152 (2014).
- Albertus, P. et al. Identifying capacity limitations in the Li/oxygen battery using experiments and modeling. *J. Electrochem. Soc.* **158**, A343–A351 (2011).
- Mahne, N., Fontaine, O., Thotiyl, M. O., Wilkening, M. & Freunberger, S. A. Mechanism and performance of lithium–oxygen batteries—A perspective. *Chem. Sci.* **8**, 6716–6729 (2017).
- Mitchell, R. R., Gallant, B. M., Thompson, C. V. & Shao-Horn, Y. All-carbon-nanofiber electrodes for high-energy rechargeable Li-O₂ batteries. *Energy Environ. Sci.* **4**, 2952–2958 (2011).
- Xiao, J. et al. Hierarchically porous graphene as a lithium–air battery electrode. *Nano Lett.* **11**, 5071–5078 (2011).
- Nomura, A., Ito, K. & Kubo, Y. CNT sheet air electrode for the development of ultra-high cell capacity in lithium–air batteries. *Sci. Rep.* **7**, 45596 (2017).
- McCloskey, B. D. et al. On the efficacy of electrocatalysis in nonaqueous Li-O₂ batteries. *J. Am. Chem. Soc.* **133**, 18038–18041 (2011).
- Xu, J.-J., Wang, Z.-L., Xu, D., Zhang, L.-L. & Zhang, X.-B. Tailoring deposition and morphology of discharge products towards high-rate and long-life lithium–oxygen batteries. *Nat. Commun.* **4**, 2438 (2013).
- Tan, G. et al. Toward highly efficient electrocatalyst for Li-O₂ batteries using biphasic N-doping cobalt@graphene multiple-capsule heterostructures. *Nano Lett.* **17**, 2959–2966 (2017).
- Ottakam Thotiyl, M. M., Freunberger, S. A., Peng, Z. & Bruce, P. G. The carbon electrode in nonaqueous Li-O₂ cells. *J. Am. Chem. Soc.* **135**, 494–500 (2012).
- Gallant, B. M. et al. Influence of Li₂O₂ morphology on oxygen reduction and evolution kinetics in Li-O₂ batteries. *Energy Environ. Sci.* **6**, 2518–2528 (2013).
- Gallant, B. M. et al. The kinetics and product characteristics of oxygen reduction and evolution in LiO₂ batteries. in Imanishi, N., Luntz, A. C. & Bruce, P. (eds) *The Lithium Air Battery: Fundamentals*, 121–158 (Springer, New York, NY, 2014).
- Itkis, D. M. et al. Reactivity of carbon in lithium–oxygen battery positive electrodes. *Nano Lett.* **13**, 4697–4701 (2013).
- Giordani, V. et al. A molten salt lithium–oxygen battery. *J. Am. Chem. Soc.* **138**, 2656–2663 (2016).
- Xia, C., Kwok, C. & Nazar, L. A high-energy-density lithium–oxygen battery based on a reversible four-electron conversion to lithium oxide. *Science* **361**, 777–781 (2018).
- Kwon, H.-M. et al. Stability of glyme solvate ionic liquid as an electrolyte for rechargeable Li-O₂ batteries. *ACS Appl. Mater. Interfaces* **9**, 6014–6021 (2017).
- Zhao, Q. et al. Binary mixtures of highly concentrated tetraglyme and hydrofluoroether as a stable and nonflammable electrolyte for Li-O₂ batteries. *ACS Appl. Mater. Interfaces* **10**, 26312–26319 (2018).
- Li, F. & Chen, J. Mechanistic evolution of aprotic lithium–oxygen batteries. *Adv. Energy Mater.* **7**, 1602934 (2017).
- Lacey, M. J., Frith, J. T. & Owen, J. R. A redox shuttle to facilitate oxygen reduction in the lithium air battery. *Electrochem. Commun.* **26**, 74–76 (2013).
- Yang, L., Frith, J., Garcia-Araez, N. & Owen, J. R. A new method to prevent degradation of lithium–oxygen batteries: reduction of superoxide by viologen. *Chem. Commun.* **51**, 1705–1708 (2015).
- Qu, L., Liu, Y., Baek, J.-B. & Dai, L. Nitrogen-doped graphene as efficient metal-free electrocatalyst for oxygen reduction in fuel cells. *ACS Nano* **4**, 1321–1326 (2010).
- Back, S. & Siahrostami, S. Noble metal supported hexagonal boron nitride for the oxygen reduction reaction: a DFT study. *Nanoscale Adv.* **2**, 15–26 (2018).
- Kwak, W.-J. et al. A Mo₂C/carbon nanotube composite cathode for lithium–oxygen batteries with high energy efficiency and long cycle life. *ACS Nano* **9**, 4129–4137 (2015).
- Soundiraraju, B. & George, B. K. Two-dimensional titanium nitride (Ti₂N) MXene: synthesis, characterization, and potential application as surface-enhanced Raman scattering substrate. *ACS Nano* **11**, 8892–8900 (2017).
- Naguib, M. et al. Two-dimensional nanocrystals produced by exfoliation of Ti₃AlC₂. *Adv. Mater.* **23**, 4248–4253 (2011).
- Anasori, B. et al. Experimental and theoretical characterization of ordered MAX phases Mo₂TiAlC₂ and Mo₂Ti₂AlC₃. *J. Appl. Phys.* **118**, 094304 (2015).
- Halim, J. et al. Synthesis and characterization of 2D molybdenum carbide (MXene). *Adv. Funct. Mater.* **26**, 3118–3127 (2016).
- Seh, Z. W. et al. Two-dimensional molybdenum carbide (MXene) as an efficient electrocatalyst for hydrogen evolution. *ACS Energy Lett.* **1**, 589–594 (2016).
- Lipatov, A. et al. Effect of synthesis on quality, electronic properties and environmental stability of individual monolayer Ti₃C₂ MXene flakes. *Adv. Electron. Mater.* **2**, 1600255 (2016).
- Anasori, B., Lukatskaya, M. R. & Gogotsi, Y. 2d metal carbides and nitrides (MXenes) for energy storage. *Nat. Rev. Mater.* **2**, 1–17 (2017).
- Ling, C., Shi, L., Ouyang, Y., Chen, Q. & Wang, J. Transition metal-promoted V₂CO₂ (MXenes): a new and highly active catalyst for hydrogen evolution reaction. *Advanced Science* **3**, 1600180 (2016).
- Khazaei, M., Arai, M., Sasaki, T., Estili, M. & Sakka, Y. Trends in electronic structures and structural properties of MAX phases: a first-principles study on M₂AlC (M = Sc, Ti, Cr, Zr, Nb, Mo, Hf, or Ta), M₂AlN, and hypothetical M₂AlB phases. *J. Phys.: Condens. Matter* **26**, 505503 (2014).
- Lipatov, A. et al. Elastic properties of 2D Ti₃C₂T_x MXene monolayers and bilayers. *Sci. Adv.* **4**, eaat0491 (2018).
- Er, D., Li, J., Naguib, M., Gogotsi, Y. & Shenoy, V. B. Ti₃C₂ MXene as a high capacity electrode material for metal (Li, Na, K, Ca) ion batteries. *ACS Appl. Mater. Interfaces* **6**, 11173–11179 (2014).
- Xie, Y. et al. Role of surface structure on Li-ion energy storage capacity of two-dimensional transition-metal carbides. *J. Am. Chem. Soc.* **136**, 6385–6394 (2014).
- Grimme, S. Semiempirical GGA-type density functional constructed with a long-range dispersion correction. *J. Comput. Chem.* **27**, 1787–1799 (2006).
- Vanderbilt, D. Soft self-consistent pseudopotentials in a generalized eigenvalue formalism. *Phys. Rev. B* **41**, 7892–7895 (1990).
- Kresse, G. & Hafner, J. Norm-conserving and ultrasoft pseudopotentials for first-row and transition elements. *J. Phys.: Condens. Matter* **6**, 8245–8257 (1994).
- Lee, A., Krishnamurthy, D. & Viswanathan, V. Exploring MXenes as cathodes for non-aqueous lithium–oxygen batteries: design rules for selectively nucleating Li₂O₂. *ChemSusChem* **11**, 1911–1918 (2018).
- Zhang, D. et al. Computational study of low interlayer friction in Ti_{n+1}C_n (n = 1, 2 and 3) MXene. *ACS Appl. Mater. Interfaces* **9**, 34467–34479 (2017).
- Yun, K.-H., Hwang, Y. & Chung, Y.-C. Effective catalytic media using graphitic nitrogen-doped site in graphene for a non-aqueous Li-O₂ battery: a density functional theory study. *J. Power Sources* **277**, 222–227 (2015).
- Jing, Y. & Zhou, Z. Computational insights into oxygen reduction reaction and initial Li₂O₂ nucleation on pristine and N-doped graphene in Li-O₂ batteries. *ACS Catal.* **5**, 4309–4317 (2015).
- Song, K. et al. Anisotropic surface modulation of Pt catalysts for highly reversible Li-O₂ batteries: high index facet as a critical descriptor. *ACS Catal.* **8**, 9006–9015 (2018).
- Lee, M., Hwang, Y., Yun, K.-H. & Chung, Y.-C. Cathode reaction mechanism on the h-BN/Ni (111) heterostructure for the lithium–oxygen battery. *J. Power Sources* **307**, 379–384 (2016).
- van Duin, A. C. T., Dasgupta, S., Lorant, F. & Goddard, W. A. ReaxFF: a reactive force field for hydrocarbons. *J. Phys. Chem. A* **105**, 9396–9409 (2001).
- Senftle, T. P., Meyer, R. J., Janik, M. J. & van Duin, A. C. Development of a ReaxFF potential for Pd/O and application to palladium oxide formation. *J. Chem. Phys.* **139**, 044109 (2013).
- Senftle, T. P., van Duin, A. C. & Janik, M. J. Methane activation at the Pd/CeO₂ interface. *ACS Catal.* **7**, 327–332 (2016).
- Nielson, K. D., van Duin, A. C., Oxgaard, J., Deng, W.-Q. & Goddard, W. A. Development of the ReaxFF reactive force field for describing transition metal catalyzed reactions, with application to the initial stages of the catalytic formation of carbon nanotubes. *J. Phys. Chem. A* **109**, 493–499 (2005).
- Osti, N. C. et al. Effect of metal ion intercalation on the structure of MXene and water dynamics on its internal surfaces. *ACS Appl. Mater. Interfaces* **8**, 8859–8863 (2016).
- Jiang, J. et al. Ruthenium functionalized graphene aerogels with hierarchical and three-dimensional porosity as a free-standing cathode for rechargeable lithium–oxygen batteries. *NPG Asia Mater.* **8**, 239 (2016).
- Black, R. et al. Screening for superoxide reactivity in Li-O₂ batteries: effect on Li₂O₂/LiOH crystallization. *J. Am. Chem. Soc.* **134**, 2902–2905 (2012).
- Zhai, D. et al. Disproportionation in Li-O₂ batteries based on a large surface area carbon cathode. *J. Am. Chem. Soc.* **135**, 15364–15372 (2013).
- Parthasarathy, A., Srinivasan, S., Appleby, A. J. & Martin, C. R. Pressure dependence of the oxygen reduction reaction at the platinum microelectrode/nafion interface: electrode kinetics and mass transport. *J. Electrochem. Soc.* **139**, 2856–2862 (1992).
- Kulkarni, A., Siahrostami, S., Patel, A. & Nørskov, J. K. Understanding catalytic activity trends in the oxygen reduction reaction. *Chem. Rev.* **118**, 2302–2312 (2018).
- Xu, Y. & Shelton, W. A. O₂ reduction by lithium on Au(111) and Pt(111). *J. Chem. Phys.* **133**, 024703 (2010).
- Blöchl, P. E. Projector augmented-wave method. *Phys. Rev. B* **50**, 17953 (1994).
- Monkhorst, H. J. & Pack, J. D. Special points for Brillouin-zone integrations. *Phys. Rev. B* **13**, 5188 (1976).

63. Lee, M., Hwang, Y., Yun, K.-H. & Chung, Y.-C. Greatly improved electrochemical performance of lithium–oxygen batteries with a bimetallic platinum–copper alloy catalyst. *J. Power Sources* **288**, 296–301 (2015).
64. Aktulga, H. M., Fogarty, J. C., Pandit, S. A. & Grama, A. Y. Parallel reactive molecular dynamics: numerical methods and algorithmic techniques. *Parallel Comput.* **38**, 245–259 (2012).
65. Plimpton, S. Fast parallel algorithms for short-range molecular dynamics. *J. Comput. Phys.* **117**, 1–19 (1995).
66. Newsome, D. A., Sengupta, D. & van Duin, A. C. T. High-temperature oxidation of SiC-based composite: rate constant calculation from ReaxFF MD simulations, Part II. *J. Phys. Chem. C* **117**, 5014–5027 (2013).

Acknowledgements

The authors acknowledge the Center for Mechanistic Control of Water-Hydrocarbon-Rock Interactions in Unconventional and Tight Oil Formations, an Energy Frontier Research Center funded by the U.S. Department of Energy, Office of Science, Office of Basic Energy Sciences, and the Donors of the American Chemical Society Petroleum Research Fund for partial support of this research. M.I. acknowledges support through the DFG Mercator Fellowship SPP1980 'SpraySyn: Nanopartikelsynthese in Sprayflammen'. We benefited from fruitful discussions with Y. Gogotsi and M. Lukatskaya. This research used resources of the National Energy Research Scientific Computing Center, a DOE Office of Science User Facility supported by the Office of Science of the U.S. Department of Energy under Contract No. DE-AC02-05CH11231.

Author contributions

M.I. and A.O. designed the research. A.O. developed ReaxFF parameters, performed DFT and rMD simulations. A.O., J.G., and M.I. collaboratively analyzed the data. F.S. contributed to the interpretation of the results. A.O. and M.I. wrote the paper and prepared revisions.

Additional information

Supplementary information accompanies this paper at <https://doi.org/10.1038/s42004-019-0196-2>.

Competing interests: The authors declare no competing interests.

Reprints and permission information is available online at <http://npg.nature.com/reprintsandpermissions/>

Publisher's note: Springer Nature remains neutral with regard to jurisdictional claims in published maps and institutional affiliations.



Open Access This article is licensed under a Creative Commons Attribution 4.0 International License, which permits use, sharing, adaptation, distribution and reproduction in any medium or format, as long as you give appropriate credit to the original author(s) and the source, provide a link to the Creative Commons license, and indicate if changes were made. The images or other third party material in this article are included in the article's Creative Commons license, unless indicated otherwise in a credit line to the material. If material is not included in the article's Creative Commons license and your intended use is not permitted by statutory regulation or exceeds the permitted use, you will need to obtain permission directly from the copyright holder. To view a copy of this license, visit <http://creativecommons.org/licenses/by/4.0/>.

© The Author(s) 2019